GDCh Research Article Angewandte International Edition Chemie www.angewandte.org

How to cite: *Angew. Chem. Int. Ed.* **2025**, e20730
doi.org/10.1002/anie.202520730

Nitrate Reduction

Low-Valent Single-Atom Indium Site Regulating Ionic Interference and Adsorbed Hydrogen for Near-Unity Electrosynthesis of Ammonia

Quan Quan, Yuxuan Zhang, Boxiang Gao, Haifan Li, Dong Chen, Pengshan Xie, Weijun Wang, Dengji Li, Yi Shen, Yan Yan, Shaohai Li, Chun-Yuen Wong, SenPo Yip, and Johnny C. Ho**

Abstract: Microenvironment modulation, involving the selective adsorption of ions and the engineering of hydrogen radicals, is critical for the neutral electrochemical reduction of nitrate to ammonia at high current densities. In this work, self-adaptive low-valent indium single atoms SAs decorated copper-based nanosheets were investigated as a prototype. The catalyst exhibits a maximum ammonia Faradaic efficiency (FE_{NH3}) of 99.36% and a high NH_3 yield rate of 29.02 mg h^{-1} $mg_{cat.}^{-1}$ in neutral electrolyte. In-depth experiments and theoretical calculations suggest that the indium SAs optimize the local electronic distribution of the derived Cu matrix through strong p-d orbital couplings, with the electron-relay effect, thereby enhancing electron transfer and regulating the supply of hydrogen radicals to accelerate the hydrogenation process. Furthermore, in situ Raman results and molecular dynamics simulations reveal that the indium SAs can act as solid-state buffering sites by inducing a potential-dependent adsorption behavior of NO_3^- over SO_4^{2-} as a supporting oxoanion in the electric double layer, consequently maintaining high reaction activity and selectivity. Herein, the as-designed electrode operates stably at 200 mA cm^{-2} for 150 h in a bipolar membrane electrode assembly electrolyzer with a FE_{NH3} of ~83%, indicating promising practical applications.

Introduction

Ammonia (NH_3) is a vital feedstock in the industrial production of fertilizers, synthetic fibers, and pharmaceuticals.[1] To date, industrial-scale NH_3 production still relies on the Haber–Bosch technology, an energy-intensive process characterized by high temperatures and pressures, which is accompanied by significant carbon dioxide emissions.[2] Furthermore, the increasing levels of anthropogenic nitrogen fixation have disrupted the natural nitrogen cycle on Earth, leading to the accumulation of harmful nitrate (NO^{3-}) contamination in groundwater and posing significant environmental and health risks. Recently, eco-friendly electrochemical nitrate reduction reaction (NO_3^-RR) has shown significant potential for achieving sustainable NH_3 production and wastewater purification at ambient conditions.[3] Fundamentally, the electrosynthesis of NH_3 is a complex proton-coupled electron transfer cascade process involving eight electrons and water dissociation to form adsorbed hydrogen radical (*H) in neutral and alkaline medium, followed by the sequential hydrogenation of adsorbed NO_3^- and intermediates,[4] thus requiring continued research into the advanced catalyst design and meticulous microenvironment modulation.[5]

The NH_3 yield rate and selectivity are primarily determined by the dynamic equilibrium between *H generation and consumption, related to the coupling behavior with nitrogenous intermediates or other *H in the NO_3^-RR processes.[6] For instance, benefiting from the highly occupied d-orbital electrons, transition metal electrocatalysts have been widely explored, especially for Cu-based nanomaterials, which exhibit a superior affinity for NO_3^- ions.[7–12] However, this feature concomitantly enhances the *H binding, aggravating the parasitic hydrogen evolution reaction (HER). In this regard, p-block metal elements with weak *H binding are investigated as hetero-dopants or modifiers to manipulate the generation and coverage of *H over Cu-based catalysts,

[*] Q. Quan, Y. Zhang, B. Gao, D. Chen, P. Xie, W. Wang, D. Li, Y. Shen, Y. Yan, J. C. Ho
Department of Materials Science and Engineering, City University of Hong Kong, Hong Kong, SAR 999077, China
E-mail: johnnyho@cityu.edu.hk

H. Li, C.-Y. Wong
Department of Chemistry, City University of Hong Kong, Hong Kong, SAR 999077, China

J. C. Ho
State Key Laboratory of Terahertz and Millimeter Waves, City University of Hong Kong, Hong Kong, SAR 999077, China

S. Li
Institute of Materials Research, Tsinghua Shenzhen International Graduate School, Tsinghua University, Shenzhen 518055, China
E-mail: sh09.li@nus.edu.sg

S. Yip, J. C. Ho
Institute for Materials Chemistry and Engineering, Kyushu University, Fukuoka 816-8580, Japan

S. Li
Department of Materials Science and Engineering, National University of Singapore, Singapore 117574, Singapore

J. C. Ho
City University of Hong Kong (Dongguan), Dongguan 523000, China

Additional supporting information can be found online in the Supporting Information section

steering the specific hydrogenation pathway.[13] Nevertheless, the effective dynamics control of the *H is still limited due to the rapid consumption of NO_3^- ions at high reaction rate, resulting in severe concentration polarization of the electric double layer (EDL).[14] Especially in neutral wastewater, the NO_3^-RR is constrained by the weak adsorption affinity of NO_3^- ions due to the electrostatic repulsion at the electrolyte-electrode interface and the coexisting competitive anionic adsorption with the supporting ions,[15] thus affecting the kinetics and pathways of NO_3^-RR.[16] For instance, sulfate (SO_4^{2-}) ions are common components in industrial effluents. They are widely applied as supporting electrolytes in neutral NO_3^-RR, which can induce negative ionic interference in the space of the EDL. Currently, the synergistic regulation of *H intermediate and the selective adsorption of NO_3^- in microenvironments remains underexplored.

In this work, as a proof of concept, we first synthesized p-block In single atoms (SAs) dispersed in ultrathin cuprous oxide nanosheets (Cu_2O-In_{SA}) through in situ topological reconstruction of bimetallic coordination polymer nanosheets. In a neutral medium using KNO_3 and Na_2SO_4, the obtained catalyst can achieve a maximum NH_3 Faradaic efficiency (FE_{NH3}) of 99.36%, an NH_3 yield rate of 29.02 mg h^{-1} $mg_{cat.}^{-1}$, and excellent electrocatalytic stability over 30 cycles for the NO_3^-RR. In situ and ex situ experiments, as well as theoretical calculations, highlight that the low-valent In SAs, when decorating the oxide-derived Cu nanosheets with strong p-d orbital couplings through self-adaptive reconstruction of Cu_2O-In_{SA}, can enhance the electron transfer, favor the supply of *H, and lower the energy barrier of the rate-determining protonation step. Meanwhile, the in situ Raman spectra and molecular dynamics (MD) simulations confirm that the In SAs in the oxide-derived Cu matrix can act as a solid-state buffer to effectively intensify the interfacial adsorption of NO_3^- ions by repelling the SO_4^{2-} ions as the NO_3^-RR reaction proceeds with continuous NO_3^- ions consumption, further ensuring the high efficiency of ammonia production during the NO_3^-RR. In this regard, the as-obtained electrocatalyst can operate stably at 200 mA cm^{-2} for 150 h by applying a bipolar membrane electrode assembly electrolyzer with a sustained FE_{NH3} of ~83%. It can also be efficiently driven by a solar cell under sunlight irradiation for NH_3 synthesis, demonstrating its promising practical application potential.

Results and Discussion

Catalyst Synthesis and Characterization

The synthesis process of Cu_2O-In_{SA} is illustrated in Figure 1a, which involves a cation exchange reaction followed by an in situ electrochemical reconstruction process. First, the 2D indium coordination polymers (In CPs) nanosheets were synthesized with bismuthiol I ($C_2H_2N_2S_3$) as ligand units through a weak reductant-induced polymerization process (Figure S1).[17] The In atom centers were then controllably substituted by Cu^{2+} cations to synthesize the Cu–In bimetallic coordination polymers (denoted as Cu–In CPs). The corresponding transmission electron microscopy (TEM) image and energy-dispersive X-ray spectra (EDS) mapping reveal the well-dispersed Cu, In, N, and S elements in the Cu–In CPs nanosheets (Figure 1b). The atomic force microscopy (AFM) image discloses a thickness of ~4.3 nm for Cu–In CPs nanosheets (Figure S2). Afterward, the In SAs embedded Cu_2O nanosheets were synthesized via electrochemistry-induced topological reconstruction of the Cu–In CPs with ligand unit detachments. The Cu_2O-In_{SA} sample well maintains the 2D structure and exhibits apparent transparency under electron beam irradiation (Figure 1c). The AFM image confirms the ultrathin structure of Cu_2O-In_{SA} with a thickness of ~4.0 nm (Figure 1d). To probe the detailed structure at the atomic scale, an aberration-corrected high-angle annular dark field-scanning transmission electron microscopy (AC-HAADF-STEM) image was collected on the Cu_2O-In_{SA} nanosheets (Figure 1e). The discerned lattice spacings of 0.25 nm can be assigned to the Cu_2O (111) facets. Meanwhile, the brighter dots marked by red circles indicate the presence of monodispersed In SAs.[18] Moreover, the existence of isolated In atoms was further confirmed by the profiles along the dashed rectangles in the AC-HAADF-STEM image, where different atomic intensities are clearly distinguished (Figure 1f). EDS elemental mapping images also depict a homogeneous distribution of Cu, In, and O atoms throughout the entire Cu_2O-In_{SA} sample (Figure 1g).

The component of bimetallic coordination polymer precursors can be modulated by controlling the degree of cation exchange (Figure 2a). As revealed by Raman spectra, the typical peak around 167 cm^{-1}, ascribed to the A_g^1 vibration of the In—S bond in In CPs, is decreased in In–Cu CPs; then, this peak disappears, and the typical Cu—S signal at around 470 cm^{-1} is generated in Cu–In CPs;[19,20] afterward, the Cu—S signal is intensified in the final pure Cu CPs (Figure 2b). The corresponding scanning electron microscopy (SEM) images of the samples reveal the well-maintained 2D structure of the In CPs substrate with uniform element distributions (Figures S3–S5). Meanwhile, the X-ray photoelectron spectroscopy (XPS) spectra of In 3d are weakened, left-shifted, and eventually disappear with the progressive exchange of Cu^{2+} cations (Figure 2c). In contrast, the Cu 2p spectra are gradually intensified and shifted to the right (Figure S6). In this way, the controllable Cu substitution in the structure of the In CPs during the subsequent reconstruction process provides the In atoms with tuned coordination environments, which enables the construction of atomically dispersed In sites in Cu-based nanosheets.

To monitor the structural reconstruction process of Cu–In CPs in neutral media, in situ Raman spectroscopy characterization was conducted. As the pretreatment time increases, the decreased intensity of the Raman vibration peaks ascribed to the stretch of ν(C=N) and ν(C–N) at 1370 cm^{-1} can be observed (Figures 2d and S7), demonstrating the gradual detachment of the ligand units of the bimetallic coordination polymers. The characteristic peaks at 1347 and 1602 cm^{-1} are assigned to the D and G bands of carbon black,[21] which is introduced to enhance the dispersion and conductivity of the precursors.[22] Simultaneously, the typical Cu—S bond is gradually transformed into the characteristic

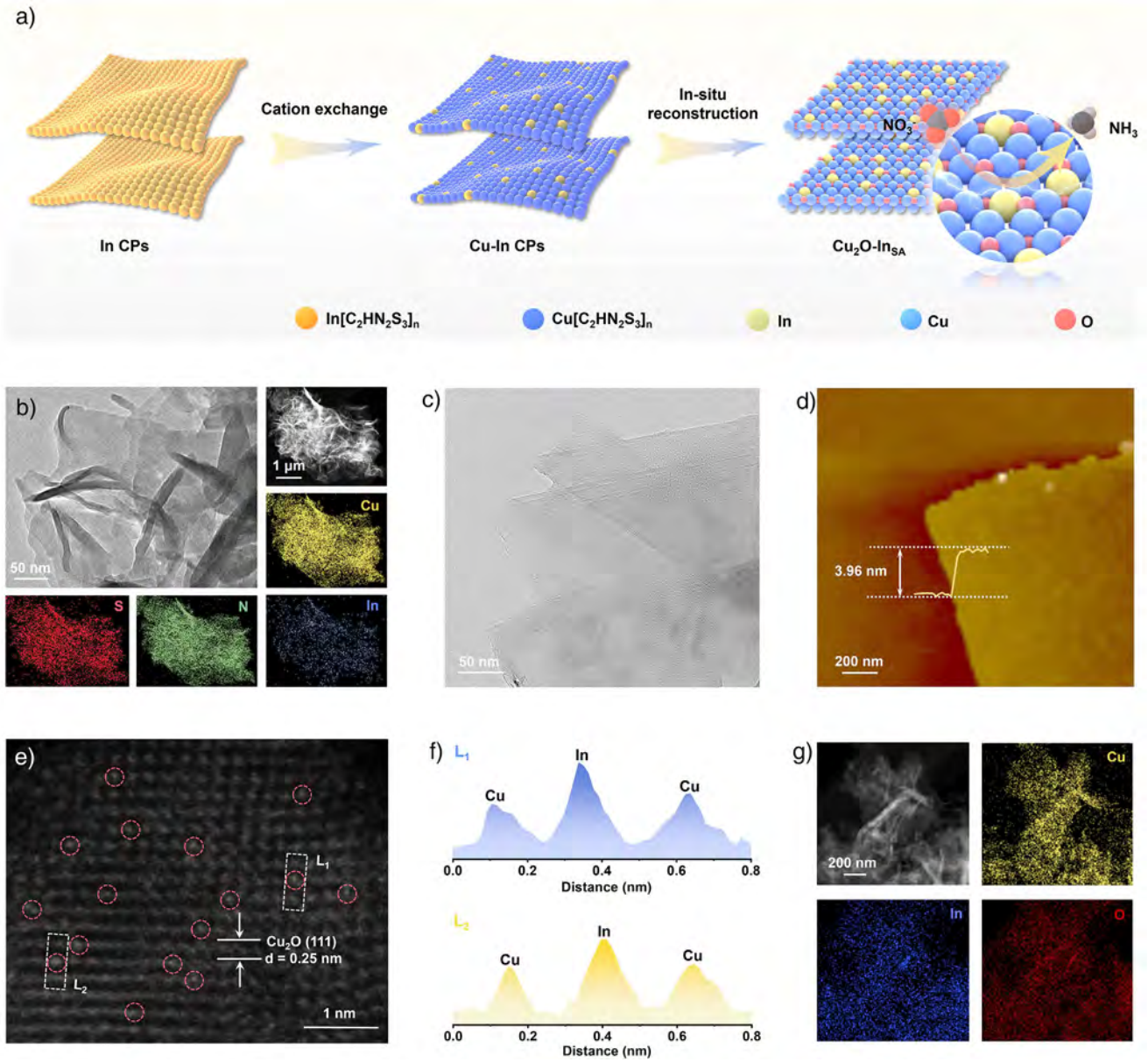

Figure 1. Synthesis of Cu_2O-In_{SA} nanosheets. a) Schematic illustration of the synthesis process of Cu_2O-In_{SA}. b) TEM, HAADF-STEM, and the corresponding EDS mapping images of the Cu–In CPs precursor. c) TEM, d) AFM, and e) AC-HADDF-STEM images of Cu_2O-In_{SA}. f) Corresponding intensity profiles. g) HADDF-STEM and the corresponding EDS mapping images of Cu_2O-In_{SA}.

Cu─O bonds at around 163, 427, and 628 cm^{-1}, which can be ascribed to the formation of Cu_2O.[23] Interestingly, the peaks corresponding to the NO_3^- ions and SO_4^{2-} ions gradually increased, indicating that the reconstructed Cu_2O-In_{SA} structure is beneficial for adsorbing oxoanions, which facilitate the subsequent reduction reaction.[24] Moreover, the depth-profiling XPS spectra of the Cu LMM Auger region of the Cu–In CPs sample after pretreatment show one strong signal at around 916 eV (Figure 2e),[25] indicating the formation of the Cu_2O phase, in agreement with the in situ Raman results.

X-ray absorption fine structure (XAFS) spectroscopy was performed to unveil the atomic coordination environment of In sites in the reconstructed Cu_2O-In_{SA}. The In *K*-edge X-ray absorption near-edge structure (XANES) spectra indicate that the absorption edge lies between In foil and In_2O_3, demonstrating the existence of positively charged $In^{\delta+}$ ($0 < \delta < 3$) in the Cu_2O (Figure 2f).[26] The low-valent feature endows the In SAs with amphiphilicity, owing to the coexistence of vacant p-orbital and lone electron pair, potentially acting as both a Lewis acid site and a Lewis base site during the NO_3^-RR.[27] The Fourier transform (FT) extended X-ray adsorption fine structure (EXAFS) spectra and the corresponding fitting results display a major peak at around 2.09 Å corresponding to the scattering of In─O bonding and no scattering peaks for In–In metallic bonding is detected (Figure 2g and Table S1), indicating that the In species is in an isolated atomic state in the lattice of Cu_2O

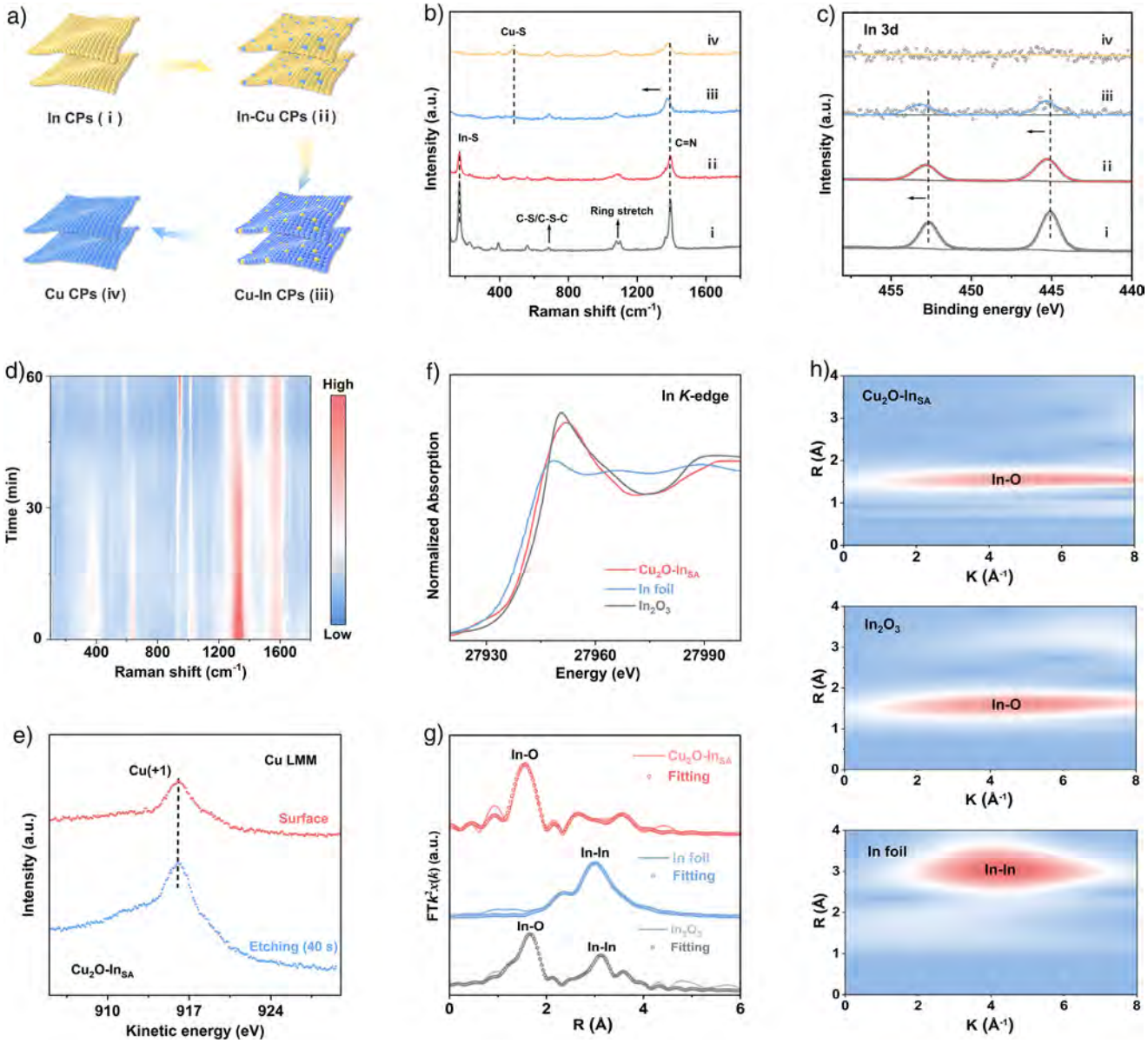

Figure 2. Atomic structural and chemical states analysis. a) Schematic illustration of the gradient cation exchange strategy. Raman spectra (b) and In 3d XPS spectra (c) of In CPs, In-Cu CPs, Cu–In CPs, and Cu CPs. d) Contour plot of in situ Raman spectra for the reconstruction process of Cu–In CPs into Cu_2O-In_{SA}. e) Depth-profiling Cu LMM Auger spectra for Cu_2O-In_{SA}. In *K*-edge XANES spectra (f) and FT k^3-weighted EXAFS spectra (g) of Cu_2O-In_{SA} and reference samples. h) EXAFS wavelet transform plots.

nanosheets,[28] which is further confirmed by the Wavelet transform plots (Figure 2h).

To further disclose the effect of the structural evolution on the adsorption behavior toward NO_3^- ions, the in situ Raman spectroscopy over the Cu CPs, In CPs, and In–Cu CPs precursors was performed under identical conditions. For the Cu CPs, the bonds ascribed to Cu_2O at around 163, 446, and 637 cm^{-1} are generated, accompanied by the detachment of the ligand units, demonstrating that the Cu CPs precursor is reconstructed into Cu_2O (Figure S8). The corresponding depth-profiling XPS spectra of the Cu LMM Auger region confirm the formation of Cu (+1) species (Figure S9). Moreover, the negative shift of Cu $2p_{3/2}$ and Cu $2p_{1/2}$ peaks of Cu_2O-In_{SA} compared to the Cu_2O counterparts implies the strong electron interaction between In SAs and Cu_2O (Figure S10).[29] Besides, the reconstruction process of Cu CPs also exhibits gradually enhanced oxoanion adsorption corresponding to the NO_3^- and SO_4^{2-} ions, which is similar to that of Cu–In CPs, suggesting that the derived Cu_2O and Cu_2O-In_{SA} catalysts engender a larger number of adsorption sites toward NO_3^- ions. In addition, the In CPs and In-Cu CPs precursors are reconstructed into amorphous InO_x and Cu-InO_x, which are corroborated by the corresponding in situ Raman spectroscopy and XPS results (Figures S11 and S12).[30] Interestingly, the In-rich CPs show strong adsorption peaks of SO_4^{2-} ions before the reconstructions, whereas no obvious Raman peaks of oxoanion are detected over the derived InO_x and Cu-InO_x.[31] Therefore, the

above findings suggest that the synergetic In/Cu sites with specific chemical environments can potentially modulate the adsorption behaviors and the interfacial concentration of the oxoanions, which will be further explored and verified in detail.

Electrocatalytic Performance of NO_3^-RR

In the following, electrochemical NO_3^-RR measurements were conducted using a three-electrode system in an H-cell at room temperature with a 0.5 M Na_2SO_4 solution containing 0.1 M KNO_3 as electrolyte. The products were quantified by ultraviolet–visible spectroscopy (UV–vis) (Figures S13 and S14).[32] The Cu_2O-In_{SA} sample and the other three counterparts (i.e., InO_x, Cu-InO_x, and Cu_2O) were evaluated for the performance of NO_3^-RR to NH_3. As depicted in the linear sweep voltammetry (LSV) curves (Figure 3a), the current densities of all samples are enhanced after adding the NO_3^- ions, suggesting that the NO_3^-RR is relatively active compared to the competitive HER. Notably, the increased current densities of Cu_2O-In_{SA} and Cu_2O are more pronounced than those of the InO_x and Cu-InO_x, suggesting that affluent Cu sites are auspicious to the NO_3^-RR. Additionally, the Cu_2O-In_{SA} electrocatalyst exhibits higher current density than Cu_2O in the presence or absence of NO_3^- ions, demonstrating that the In SAs can enhance the electrochemical NO_3^-RR capability of Cu_2O. As shown in Figure 3b,c, the Cu_2O-In_{SA} sample also exhibits superior Faradaic efficiency (FE) and yield rate for electrocatalytic conversion of NO_3^- to NH_3. Specifically, at −0.8 V versus RHE, Cu_2O-In_{SA} presents a FE_{NH3} of 99.36% with an NH_3 yield rate of 23.37 mg h^{-1} $mg_{cat.}^{-1}$. Besides, an impressive NH_3 yield rate of 29.02 mg h^{-1} $mg_{cat.}^{-1}$ can also be achieved at −0.9 V versus RHE, with a FE_{NH3} of 95.60%. In addition, the InO_x and Cu-InO_x counterparts exhibit much higher NO_2^- FE than the Cu_2O and Cu_2O-In_{SA} (Figure S15), suggesting that the affluent Cu sites are favorable for triggering water dissociation to promote the *H formation for hydrogenation of nitrogen-containing intermediates to NH_3.[33] To investigate the effect of concentration and the existing form of In species on the catalytic performance, the physically mixed InO_x-Cu_2O sample and other In SAs-related catalysts were further investigated (Figures S16–S20). The residual and excessive InO_x both deteriorate the activity, indicating that the In SA catalyst with a built-in optimized electronic structure is favorable for the NH_3 generation. Moreover, the double-layer capacitance (C_{dl}) value of Cu_2O-In_{SA} is measured to be 7.39 mF cm^{-2}, which is superior to that of Cu_2O (4.18 mF cm^{-2}), Cu-InO_x (1.99 mF cm^{-2}), and InO_x (1.20 mF cm^{-2}) (Figures S21 and S22), indicating high electrochemically surface areas and rich catalytically active sites on Cu_2O-In_{SA}.

Furthermore, the ^{15}N isotope labeling experiments were implemented to certify the sources of the NH_3 product (Figure 3d). The ^1H nuclear magnetic resonance (^1H NMR) spectrum of the product displays triple peaks when $K^{14}NO_3$ is adopted as a reactant. The ^1H NMR spectrum exhibits double peaks of $^{15}NH_4^+$ in the case of $K^{15}NO_3$ as the feedstock, confirming that the detected NH_3 product comes from the electrochemical NO_3^-RR process rather than the contamination. Meanwhile, based on the NMR quantification method of $^{15}NH_3$ (Figure S23), the value of generated $^{15}NH_3$ from electrolyzing $K^{15}NO_3$ at −0.8 V versus RHE is very close to the result measured by the UV–vis method (Figure 3e), corroborating the reliability of the NH_3 production measurements. To highlight the durability of Cu_2O-In_{SA} for the NO_3^-RR, a consecutive cycling test was performed (Figure S24). The Cu_2O-In_{SA} can maintain a high FE_{NH3} and NH_3 yield rate with only slight fluctuations after 30 consecutive cycles. XPS analysis reveals that the signals in the In 3d region exhibit no discernible shift, indicating the stable chemical state of In SAs during long-term operation, without the formation of metallic In aggregation (Figure S25). In those regards, the overall performance of Cu_2O-In_{SA} ranks in the top tier among the recently reported state-of-the-art electrocatalysts for NO_3^-RR (Figure 3f; Tables S2 and S3).

To further demonstrate the large-scale application potential of the Cu_2O-In_{SA} electrocatalyst for ammonia synthesis, we assembled the Cu_2O-In_{SA} electrode within a high-throughput bipolar membrane electrode assembly (MEA) reactor (Figure 3g). Specifically, we spray-coated Cu_2O-In_{SA} on carbon fiber paper (CFP) as a cathode. We selected a commercial NiFeO/Ni fiber as an anode. The potentiostatic experiment was conducted with 0.5 M Na_2SO_4 and 0.1 M KNO_3 as the catholyte and 1 M KOH as the anolyte. The utilization of a bipolar membrane can prevent the crossover of produced NH_3 to the anode from being re-oxidized again under high current density (Figure S26).[34] It is found that the reactor can maintain a steady current density-time profile at 200 mA cm^{-2} for 150 h with a high NH_3 faradaic efficiency of ~83% (Figure 3h). Additionally, a photovoltaic-electrolysis system for ammonia synthesis was also constructed through the integration of a two-electrode setup and a commercial silicon solar cell (Figure S27a). The Cu_2O-In_{SA} cathode proceeds electrocatalytic NO_3^-RR without observation of hydrogen bubbles. In contrast, many oxygen bubbles emerge on the surface of the coupled NiFeO/Ni fiber anode (Figure S27b,c). Moreover, as indicated by the indophenol blue method, ammonia production increases with prolonged reaction time (Figure S27d). Therefore, the results demonstrate that the Cu_2O-In_{SA} electrode possesses great potential for industrial ammonia synthesis applications.

Mechanism Exploration

To study the real active species in the reductive process, AC-HADDF-STEM analysis was conducted on the Cu_2O-In_{SA} after the NO_3^-RR process at −0.8 V versus RHE. The corresponding image reveals a typical lattice fringe of 0.21 nm, which can be ascribed to the (111) plane of metallic Cu (Figure 4a).[35,36] Meanwhile, the brighter dots marked by red circles demonstrate the well-maintained dispersion of In SAs. Moreover, the TEM and elemental mapping images reveal a well-sustained 2D nanosheet morphology and a well-dispersed distribution of Cu and In elements (Figure S28). The X-ray diffraction (XRD) pattern of Cu_2O-In_{SA} electrode

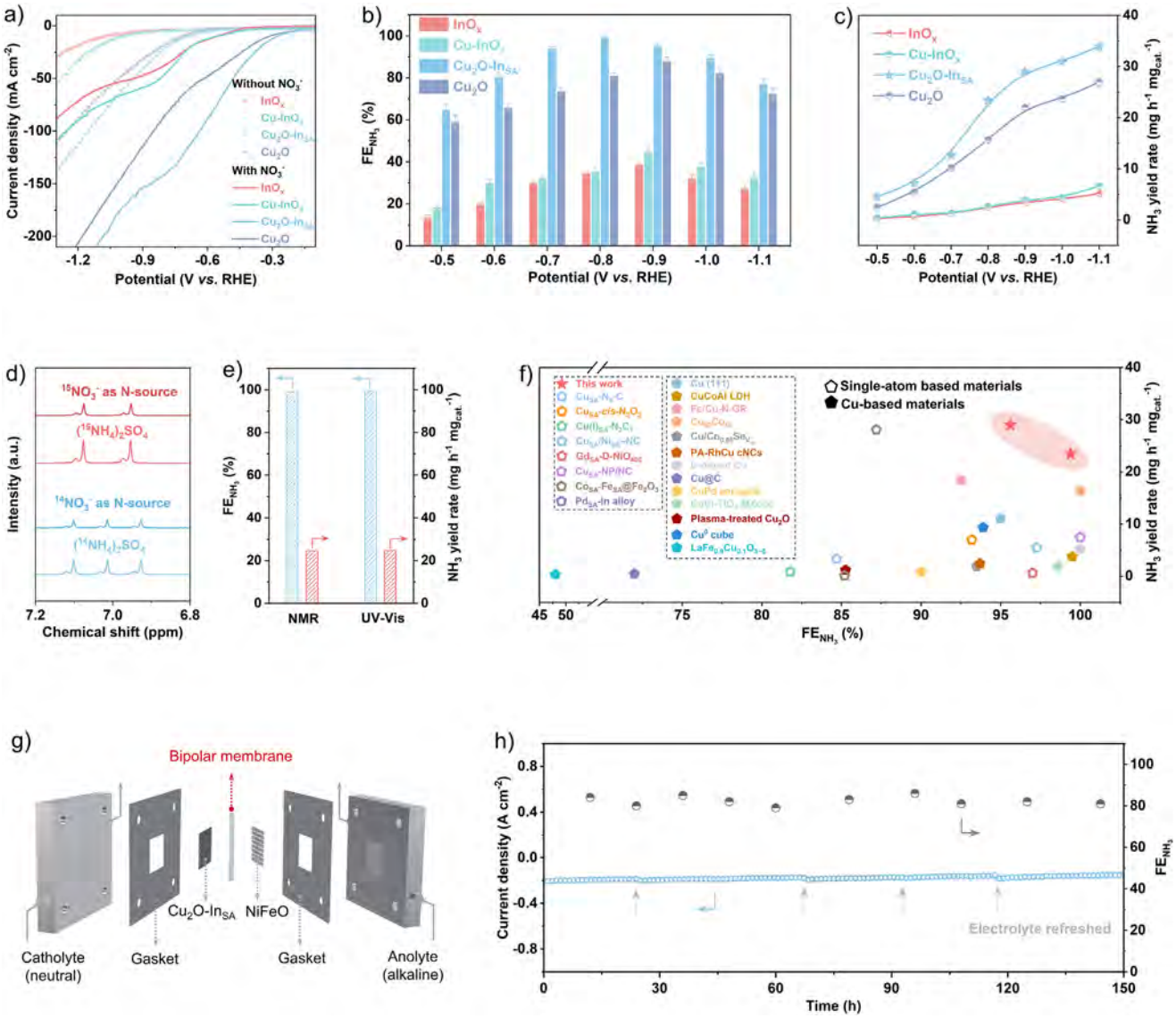

Figure 3. Electrocatalytic performance of NO_3^-RR. a) LSV curves in an electrolyte of 0.5 M Na_2SO_4 with and without 0.1 M KNO_3. b) Faradaic efficiencies for NH_3 (FE_{NH3}). c) NH_3 yield rates over the different samples (the error bars represent the standard deviations determined from three independent experimental tests). d) ^{1}H NMR spectra of electrolytes after the reaction at −0.8 V (versus RHE) using 0.1 M $^{15}NO_3^-$ and $^{14}NO_3^-$ as nitrogen sources. e) The calculated FE_{NH3} and NH_3 yield rates using the NMR and UV–vis methods. f) Comparison of the NO_3^-RR performance of the Cu_2O-In_{SA} with single-atom and Cu-based materials. g) Schematic illustration of NH_3 electrosynthesis in a bipolar membrane electrode assembly reactor. h) Time-dependent current density and FE_{NH3} over the Cu_2O-In_{SA} electrode.

after the NO_3^-RR displays the typical diffraction peak at 43° corresponding to the (111) plane of the metallic Cu phase (JCPDS no.04-0836) (Figure S29).[37] Therefore, these results reveal that the Cu_2O substrate is self-adaptively reconstructed into metallic Cu nanosheets during the NO_3^-RR process (denoted as Cu–In_{SA}) (Figure S30). Likewise, the pure Cu_2O counterpart also undergoes a reconstructed process into metallic Cu, as supported by the results of XRD and HRETM (Figures S29 and S31). Furthermore, the local fine structure of the In site in the Cu–In_{SA} was investigated using XAFS measurement. The In *K*-edge XANES spectrum of Cu–In_{SA} is exhibited in Figure 4b. The FT-EXAFS spectrum and corresponding fitting results display no In-In coordination bond at around 3.2 Å, suggesting that the In atoms maintain an atomically dispersed state without aggregation in the Cu–In_{SA} after the NO_3^-RR process (Figure 4c and Table S4).[38,39]

To unveil the role of In SAs on the interfacial selective adsorption behavior of ions during the NO_3^-RR process, the in situ Raman spectroscopy was conducted under different applied potentials (Figure S32a). The Raman characteristic peaks of the Cu_2O matrix and the adsorption behaviors toward NO_3^- ions are well preserved from open circuit potential (OCP) to −0.7 V versus RHE. After further increasing the applied negative potential, the relative intensity ratio of vibration peaks associated with the adsorption of SO_4^{2-} and NO_3^- ions exhibits apparent inversion (Figure S32b). The affinity toward SO_4^{2-} generally remains stable for the reported Cu-based catalysts as the potential becomes

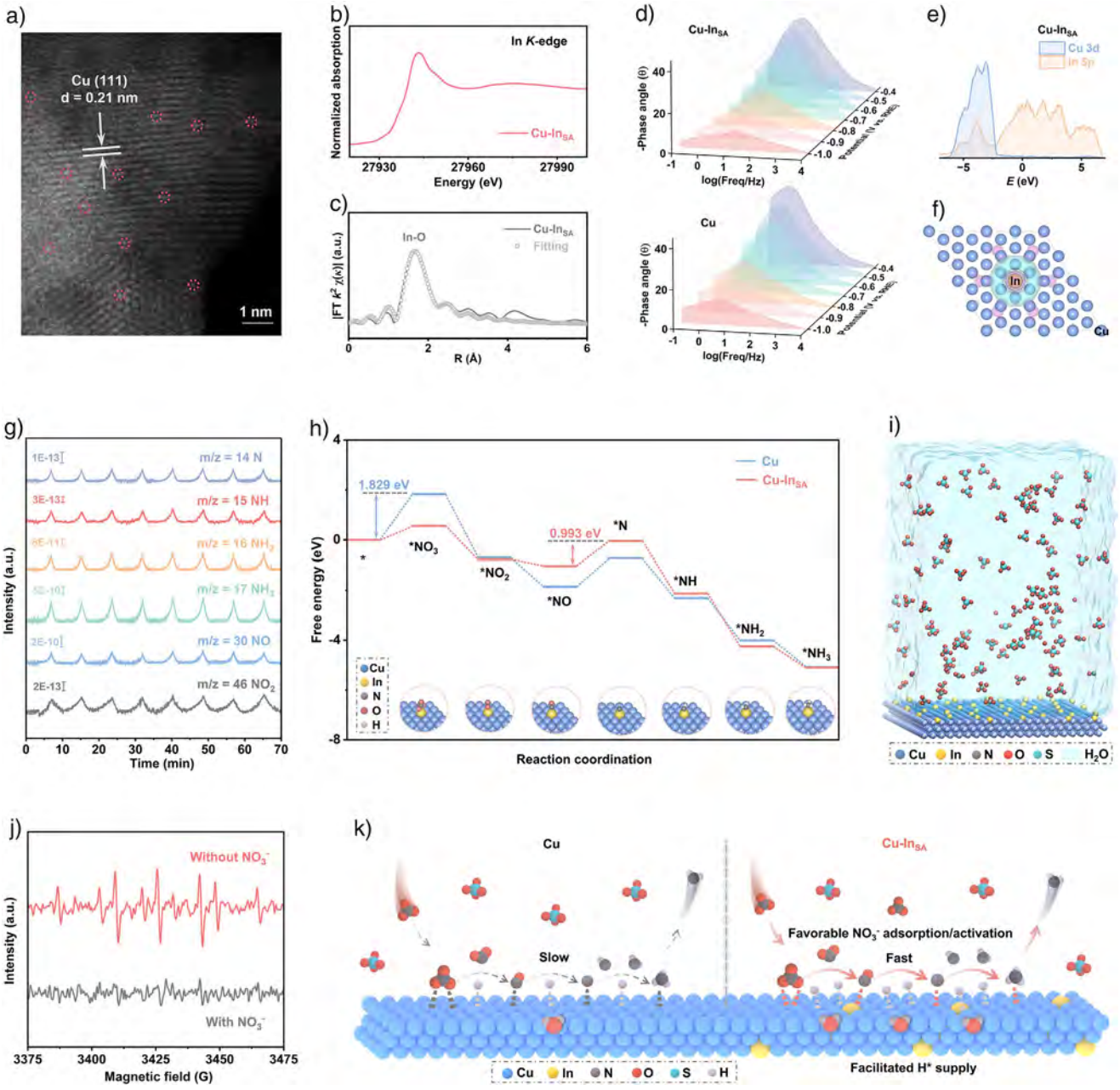

Figure 4. Insights into the NO_3^-RR to NH_3 mechanism. a) AC-HADDF-STEM of Cu_2O-In_{SA} after NO_3^-RR (i.e., Cu–In_{SA}). b) The normalized XANES at the In *K*-edge of Cu–In_{SA}. c) FT-EXAFS fitting curve of Cu–In_{SA}. d) Bode phase plots of Cu–In_{SA} and Cu at varied potentials. e) PDOS of Cu–In_{SA}. f) Charge density differences of Cu–In_{SA} (blue: electron accumulation; purple: electron depletion). g) Online DEMS measurements of NO_3^-RR over Cu–In_{SA}. h) Calculated free energy diagrams for NO_3^-RR. i) MD simulation of Cu–In_{SA} in 0.5 M Na_2SO_4 solution containing 0.1 M KNO_3. j) DMPO spin-trapping EPR spectra for *H detection toward Cu–In_{SA} with and without NO_3^-. k) Schematic diagram of NO_3^-RR to NH_3 process on Cu–In_{SA} and Cu.

increasingly negative.[40] Here, the results demonstrate a gradually pronounced NO_3^- enrichment effect with SO_4^{2-} repelling at the interface of electrode-electrolyte during the NO_3^-RR process.[16] Meanwhile, the Raman peaks belonging to Cu_2O disappear owing to its reduction to metallic Cu, which is consistent with the above observations. The new Raman peak, appropriately around 1505 cm^{-1}, assigned to -NH intermediate, appears with increased potential, verifying the hydrogenation process.[41] Moreover, it can be deduced that, from OCP to −0.7 V, the incompletely reconstrued Cu_2O-In_{SA} with residual electronegative oxygen atoms could induce a stronger electric field, which is beneficial for the Coulomb attraction of SO_4^{2-} with high localized charge density. After self-adaptively reconstructing into Cu–In_{SA}, the In SA features a vacant p-orbital (Lewis acidity) to adsorb/polarize NO_3^- and acts as a lone-pair/electron reservoir coupled to metallic Cu for electric field-guided proton-coupled electron transfer, yielding higher and more

stable NH_3 selectivity. For comparison, an analogous trend of Cu_2O phase reduced into metallic Cu phase is observed over the Cu_2O counterpart (Figure S33a). However, as negative potentials are increasingly applied, the intensity ratio of vibration peaks related to the adsorption of SO_4^{2-} and NO_3^- displays slight changes (Figure S33b), implying that the introduction of the low-valent In sites in the Cu matrix with vacant *p*-orbital and lone electron pair can effectively tune the dielectric microenvironment, thus enhancing the supplement of interfacial NO_3^- ions.

The operando electrochemical impedance spectra (EIS) were applied to explore the interfacial reaction kinetics of NO_3^-RR to NH_3 (Figure 4d). As a result, the Bode plots of Cu–In_{SA} with NO_3^- ions show smaller phase angles at low frequency and more significant declined peak intensity compared to those of Cu (derived from the Cu_2O counterparts), suggesting that the introduction of In SAs can accelerate the *H consumption with NO_3^- ions and enhance the interficial charge transfer with intensified NO_3^- adsorption during NO_3^-RR.[15] In the following, the density functional theory (DFT) calculations are conducted to investigate the underlying NO_3^-RR mechanism. The projected density of states (PDOS) of Cu–In_{SA} reveals a strong orbital overlap among Cu 3d and In 5p orbitals (Figure 4e).[42] More importantly, as compared with pure Cu (Figure S34), the introduction of In SAs induces much higher occupation near the Fermi level (E_f) for Cu–In_{SA}, which demonstrates a promoted electron transfer in Cu–In_{SA} by the strong p-d orbital coupling,[43] aligning with the operando EIS results. As depicted by the differential charge density of Cu_2O-In_{SA} with geometric optimization (Figure 4f), more electrons are delocalized around In SAs, illustrating that the In SAs regulate the local electronic distribution of the Cu matrix to tune the electron transportation and intermediate adsorption.[44] Moreover, the quantitative assessment using Bader charge discloses that the In center donates 0.34 electrons to the adjacent Cu atoms, forming a unique polarized In-Cu pair.

To gain a more comprehensive understanding of the reaction mechanism, online differential electrochemical mass spectrometry (DEMS) was employed to monitor key intermediates and products (Figures 4g and S35).[45] It reveals the *m/z* signals of 46, 30, 17, 16, 15, and 14, corresponding to *NO_2, *NO, *NH_3, *NH_2, *NH, and *N, respectively.[46] Therefore, the NO_3^-RR pathway can be proposed: the NO_3^- is initially adsorbed on the surface (*NO_3), subsequently reduced to *NO_2 and *NO; then, the *NO is protonated into *N, *NH_2, and NH_3 as the final product. Based on the DEMS results, we calculated the free energy of individual intermediates on Cu–In_{SA} and Cu (Figure 4h). The conversion from *NO to *N is identified as the rate-determining step (RDS) for Cu–In_{SA}, characterized by a lower energy barrier of 0.993 eV. At the same time, the RDS for Cu is the activation of adsorbed NO_3^- with a larger energy barrier of 1.829 eV, highlighting the critical role of In SAs in promoting the kinetics of the NO_3^-RR process.[47] Moreover, it is also indicated that the introduction of In SAs can tune the electronic structure of Cu–In_{SA} for favorable NO_3^- adsorption and activation.

Based on the above experimental and theoretical findings, molecular dynamics (MD) simulations were conducted to quantitatively analyze the dynamic behavior of NO_3^- at the interface of a Cu–In_{SA} electrode with the electrolyte in a neutral Na_2SO_4 solution (Figure 4i).[48] The pure Cu electrode was constructed as a comparison (Figure S36). The resulting radial distribution function (RDF) curves show a stronger interaction between Cu–In_{SA} and NO_3^- than that between Cu (Figure S37). The concentrations of NO_3^- distributed on the Cu–In_{SA} surface are higher than those on the Cu surface. Meanwhile, the Cu–In_{SA} can retard SO_4^{2-} ions by creating a longer distance of SO_4^{2-} accumulation from the surface as compared to that from the Cu surface. Furthermore, the Bader charge analysis reveals that NO_3^- gains more electronic charge from the Cu–In_{SA} surface than SO_4^{2-} (Figure S38), indicating a stronger interaction of NO_3^- compared to SO_4^{2-}.[49] Those results further confirm the critical role of the In sites in the Cu-based matrix in selectively adsorbing NO_3^- by repelling SO_4^{2-} at the electrocatalyst/electrolyte interface, thereby endowing the Cu–In_{SA} to act as a solid-state buffer that tunes the interfacial ion equilibrium to maintain the high kinetics of the NO_3^-RR.

Afterward, the water adsorption and dissociation processes are calculated, owing to the supply of the necessary *H for NO_3^-RR (Figure S39).[6] As a result, the Gibbs free energy change for water dissociation on Cu (1.42 eV) is higher than that of Cu–In_{SA} (1.34 eV), implying that In SAs can optimize the Cu matrix to improve water dissociation for more *H supply in the subsequent hydrogenation processes.[50] To obtain further evidence for the behaviors of active hydrogen (i.e., *H), we conducted electron paramagnetic resonance (EPR) measurements. The EPR spectra were collected in 0.5 M Na_2SO_4 with and without NO_3^-, utilizing 5,5-dimethyl-1-pyrroline-*N*-oxide (DMPO) as the agent for trapping hydrogen radicals. As depicted in Figure 4j, after adding NO_3^- to the solution, the peak intensity significantly decreases, suggesting that the produced hydrogen radicals are efficiently consumed with nitrogen-containing intermediates in the hydrogenation reactions.[51] In this way, due to the strong *d-p* orbital overlaps between Cu sites and In SAs, the self-adaptive Cu–In_{SA} system becomes favorable for NO_3^- adsorption and activation, lowers the energy barrier of RDS, promotes the water dissociation to facilitate *H supply for supporting NO_3^-RR activity (Figure 4k).

Conclusions

In summary, high-performance ultrathin In SAs-embedded Cu-based nanosheets for the NO_3^-RR to NH_3 were controllably synthesized via a facile topological electrochemical reconstruction strategy. Combining operando experiments, theoretical calculations, and MD simulations, it is found that the low-valent In SAs decorated the self-adaptive Cu-based nanosheet enable optimal local electronic distribution by strong p-d orbital couplings, thus facilitating electron transfer, accelerating *H supply, and lowering the RDS energy barrier. Meanwhile, the In SAs endow the Cu-based species as a solid-state buffer by strengthening the interfacial adsorption of the NO_3^- ion, while repelling SO_4^{2-} supporting ions when the NO_3^-RR proceeds continuously, thereby consuming NO_3^-

ions and sustaining a high NO_3^-RR kinetics. Therefore, under neutral conditions, the electrocatalyst can achieve a maximum FE_{NH3} of 99.36%, a high NH_3 yield rate of 29.02 mg h^{-1} $mg_{cat.}^{-1}$, and excellent electrocatalytic durability over 30 cycles, which ranks the top tier among the recently reported state-of-the-art electrocatalysts for NO_3^-RR. Besides, the as-designed electrode can be operated stably in an MEA electrolyzer at 200 mA cm^{-2} for 150 h with an average FE_{NH3} of ~83%. It can also be effectively driven by a solar cell under sunlight irradiation for NH_3 synthesis, demonstrating promising industrial applications.

Acknowledgements

This work was financially supported by the City University of Hong Kong (project no. 9229138, 9231502, and 9231539), the Guangdong Provincial Science and Technology Plan Project (no. 2025A0505080006), and the Guangdong Provincial Basic and Applied Basic Research Project (no. 2024B1515120005).

Conflict of Interests

The authors declare no conflict of interest.

Data Availability Statement

The data that support the findings of this study are available from the corresponding author upon reasonable request.

Keywords: Hydrogen radical · Nitrate reduction reaction · Selective adsorption · Single atom · Solid-state buffering

[1] S. Han, H. Li, T. Li, F. Chen, R. Yang, Y. Yu, B. Zhang, *Nat. Catal.* **2023**, *6*, 402–414.
[2] J. G. Chen, R. M. Crooks, L. C. Seefeldt, K. L. Bren, R. M. Bullock, M. Y. Darensbourg, P. L. Holland, B. Hoffman, M. J. Janik, A. K. Jones, M. G. Kanatzidis, P. King, K. M. Lancaster, S. V. Lymar, P. Pfromm, W. F. Schneider, R. R. Schrock, *Science* **2018**, *360*, eaar6611.
[3] H. Xu, Y. Ma, J. Chen, W.-X. Zhang, J. Yang, *Chem. Soc. Rev.* **2022**, *51*, 2710–2758.
[4] B. Zhou, L. Yu, W. Zhang, X. Liu, H. Zhang, J. Cheng, Z. Chen, H. Zhang, M. Li, Y. Shi, F. Jia, Y. Huang, L. Zhang, Z. Ai, *Angew. Chem. Int. Ed.* **2024**, *63*, e202406046.
[5] W. Wen, S. Fang, Y. Zhou, Y. Zhao, P. Li, X.-Y. Yu, *Angew. Chem. Int. Ed.* **2024**, *63*, e202408382.
[6] X. Zhang, X. Liu, Z.-F. Huang, L. Gan, S. Zhang, R. Jia, M. Ajmal, L. Pan, C. Shi, X. Zhang, G. Yang, J.-J. Zou, *Energy Environ. Sci.* **2024**, *17*, 6717–6727.
[7] L. Bai, F. Franco, J. Timoshenko, C. Rettenmaier, F. Scholten, H. S. Jeon, A. Yoon, M. Rüscher, A. Herzog, F. T. Haase, S. Kühl, S. W. Chee, A. Bergmann, R. C. Beatriz, *J. Am. Chem. Soc.* **2024**, *146*, 9665–9678.
[8] R. Daiyan, T. Tran-Phu, P. Kumar, K. Iputera, Z. Tong, J. Leverett, M. H. A. Khan, A. Asghar Esmailpour, A. Jalili, M. Lim, A. Tricoli, R.-S. Liu, X. Lu, E. Lovell, R. Amal, *Energy Environ. Sci.* **2021**, *14*, 3588–3598.
[9] J.-Y. Fang, Q.-Z. Zheng, Y.-Y. Lou, K.-M. Zhao, S.-N. Hu, G. Li, O. Akdim, X.-Y. Huang, S.-G. Sun, *Nat. Commun.* **2022**, *13*, 7899.
[10] Y. Wang, A. Xu, Z. Wang, L. Huang, J. Li, F. Li, J. Wicks, M. Luo, D.-H. Nam, C.-S. Tan, Y. Ding, J. Wu, Y. Lum, C.-T. Dinh, D. Sinton, G. Zheng, E. H. Sargent, *J. Am. Chem. Soc.* **2020**, *142*, 5702–5708.
[11] Q. Hu, S. Qi, Q. Huo, Y. Zhao, J. Sun, X. Chen, M. Lv, W. Zhou, C. Feng, X. Chai, H. Yang, C. He, *J. Am. Chem. Soc.* **2024**, *146*, 2967–2976.
[12] S. Zhang, M. Li, J. Li, Q. Song, X. Liu, *Proc. Natl. Acad. Sci. USA* **2022**, *119*, e2115504119.
[13] C. Ma, H. Zhang, J. Xia, X. Zhu, K. Qu, F. Feng, S. Han, C. He, X. Ma, G. Lin, W. Cao, X. Meng, L. Zhu, Y. Yu, A.-L. Wang, Q. Lu, *J. Am. Chem. Soc.* **2024**, *146*, 20069–20079.
[14] F.-Y. Chen, A. Elgazzar, S. Pecaut, C. Qiu, Y. Feng, S. Ashokkumar, Z. Yu, C. Sellers, S. Hao, P. Zhu, H. Wang, *Nat. Catal.* **2024**, *7*, 1032–1043.
[15] S. Liang, X. Teng, H. Xu, L. Chen, J. Shi, *Angew. Chem. Int. Ed.* **2024**, *63*, e202400206.
[16] J. Fan, L. K. Arrazolo, J. Du, H. Xu, S. Fang, Y. Liu, Z. Wu, J.-H. Kim, X. Wu, *Environ. Sci. Technol.* **2024**, *58*, 12823–12845.
[17] S. H. Li, S. Hu, H. Liu, J. Liu, X. Kang, S. Ge, Z. Zhang, Q. Yu, B. Liu, *ACS Nano* **2023**, *17*, 9338–9346.
[18] Y. Zhu, J. Wang, T. Koketsu, M. Kroschel, J.-M. Chen, S.-Y. Hsu, G. Henkelman, Z. Hu, P. Strasser, J. Ma, *Nat. Commun.* **2022**, *13*, 7754.
[19] Y. Wu, C. Liu, C. Wang, Y. Yu, Y. Shi, B. Zhang, *Nat. Commun.* **2021**, *12*, 3881.
[20] E. Rudigier, B. Barcones, I. Luck, T. Jawhari-Colin, A. Pérez-Rodrıǵuez, R. Scheer, *J. Appl. Phys.* **2004**, *95*, 5153–5158.
[21] Q. Quan, Y. Zhang, S. Li, S. Yip, W. Wang, P. Xie, D. Chen, W. Wang, D. Yin, Y. Li, B. Liu, J. C. Ho, *ACS Nano* **2024**, *18*, 1204–1213.
[22] Q. Quan, Z. Lai, Y. Bao, X. Bu, Y. Meng, W. Wang, T. Takahashi, T. Hosomi, K. Nagashima, T. Yanagida, C. Liu, J. Lu, J. C. Ho, *Small* **2021**, *17*, 2006860.
[23] M. He, Y. Wu, R. Li, Y. Wang, C. Liu, B. Zhang, *Nat. Commun.* **2023**, *14*, 5088.
[24] A. Kumar, J. Lee, M. G. Kim, B. Debnath, X. Liu, Y. Hwang, Y. Wang, X. Shao, A. R. Jadhav, Y. Liu, H. Tüysüz, H. Lee, *ACS Nano* **2022**, *16*, 15297–15309.
[25] W. Niu, T. Moehl, P. Adams, X. Zhang, R. Lefèvre, A. M. Cruz, P. Zeng, K. Kunze, W. Yang, S. D. Tilley, *Energy Environ. Sci.* **2022**, *15*, 2002–2010.
[26] E. Zhang, L. Tao, J. An, J. Zhang, L. Meng, X. Zheng, Y. Wang, N. Li, S. Du, J. Zhang, D. Wang, Y. Li, *Angew. Chem. Int. Ed.* **2022**, *61*, e202117347.
[27] J. A. J. Pardoe, A. J. Downs, *Chem. Rev.* **2007**, *107*, 2–45.
[28] Y. Guo, Z. Jin, J. Lu, L. Wei, W. Wang, Y. Huang, A. Wang, *Energy Environ. Sci.* **2023**, *16*, 5274–5283.
[29] K. Zhang, B. Li, F. Guo, N. Graham, W. He, W. Yu, *Angew. Chem. Int. Ed.* **2024**, *63*, e202411796.
[30] J. Zhang, R. Yin, Q. Shao, T. Zhu, X. Huang, *Angew. Chem. Int. Ed.* **2019**, *58*, 5609–5613.
[31] W. W. Rudolph, D. Fischer, M. R. Tomney, C. C. Pye, *Phys. Chem. Chem. Phys.* **2004**, *6*, 5145–5155.
[32] G.-F. Chen, Y. Yuan, H. Jiang, S.-Y. Ren, L.-X. Ding, L. Ma, T. Wu, J. Lu, H. Wang, *Nat. Energy* **2020**, *5*, 605–613.
[33] Y. Wang, F. Hao, H. Xu, M. Sun, X. Wang, Y. Xiong, J. Zhou, F. Liu, Y. Hu, Y. Ma, X. Meng, L. Guo, C. Wang, M. Shao, G. Wang, J. Wang, P. Lu, J. Yin, J. Wang, W. Niu, C. Ye, Q. Zhang, S. Xi, B. Huang, M. Shao, Z. Fan, *Angew. Chem. Int. Ed.* **2025**, *64*, e202508617.
[34] Z. Xu, L. Wan, Y. Liao, M. Pang, Q. Xu, P. Wang, B. Wang, *Nat. Commun.* **2023**, *14*, 1619.

[35] B. Zhang, J. Zhang, M. Hua, Q. Wan, Z. Su, X. Tan, L. Liu, F. Zhang, G. Chen, D. Tan, X. Cheng, B. Han, L. Zheng, G. Mo, *J. Am. Chem. Soc.* **2020**, *142*, 13606–13613.
[36] W. Luc, X. Fu, J. Shi, J.-J. Lv, M. Jouny, B. H. Ko, Y. Xu, Q. Tu, X. Hu, J. Wu, Q. Yue, Y. Liu, F. Jiao, Y. Kang, *Nat. Catal.* **2019**, *2*, 423–430.
[37] Y. Pan, Y. Li, C.-L. Dong, Y.-C. Huang, J. Wu, J. Shi, Y. Lu, M. Yang, S. Wang, Y. Zou, *Chem* **2023**, *9*, 963–977.
[38] M. Li, K. Duanmu, C. Wan, T. Cheng, L. Zhang, S. Dai, W. Chen, Z. Zhao, P. Li, H. Fei, Y. Zhu, R. Yu, J. Luo, K. Zang, Z. Lin, M. Ding, J. Huang, H. Sun, J. Guo, X. Pan, W. A. Goddard, P. Sautet, Y. Huang, X. Duan, *Nat. Catal.* **2019**, *2*, 495–503.
[39] M. Wang, M. Fang, Y. Liu, C. Chen, Y. Zhang, S. Jia, H. Wu, M. He, B. Han, *J. Am. Chem. Soc.* **2025**, *147*, 16450–16458.
[40] R. Zhao, Q. Yan, L. Yu, T. Yan, X. Zhu, Z. Zhao, L. Liu, J. Xi, *Adv. Mater.* **2023**, *35*, 2306633.
[41] S. Liu, T. Qian, M. Wang, H. Ji, X. Shen, C. Wang, C. Yan, *Nat. Catal.* **2021**, *4*, 322–331.
[42] Z. Zeng, L. Y. Gan, H. Bin Yang, X. Su, J. Gao, W. Liu, H. Matsumoto, J. Gong, J. Zhang, W. Cai, Z. Zhang, Y. Yan, B. Liu, P. Chen, *Nat. Commun.* **2021**, *12*, 4088.
[43] Q. Quan, Y. Zhang, H. Li, W. Wang, P. Xie, D. Chen, W. Wang, Y. Meng, D. Yin, Y. Li, D. Song, L. Chen, S. Li, C. Yang, T. Yanagida, C.-Y. Wong, S. Yip, J. C. Ho, *Nat. Commun.* **2025**, *16*, 2908.
[44] G. Zhang, F. Wang, K. Chen, J. Kang, K. Chu, *Adv. Funct. Mater.* **2024**, *34*, 2305372.
[45] J. Dai, Y. Tong, L. Zhao, Z. Hu, C.-T. Chen, C.-Y. Kuo, G. Zhan, J. Wang, X. Zou, Q. Zheng, W. Hou, R. Wang, K. Wang, R. Zhao, X.-K. Gu, Y. Yao, L. Zhang, *Nat. Commun.* **2024**, *15*, 88.
[46] H. Yin, Z. Chen, S. Xiong, J. Chen, C. Wang, R. Wang, Y. Kuwahara, J. Luo, H. Yamashita, Y. Peng, J. Li, *Chem Catalysis* **2021**, *1*, 1088–1103.
[47] K. Fan, W. Xie, J. Li, Y. Sun, P. Xu, Y. Tang, Z. Li, M. Shao, *Nat. Commun.* **2022**, *13*, 7958.
[48] R. Zhang, X. Ma, S. Zhang, H. Cui, C. Li, Y. Wang, Q. Li, C. Peng, Y. Guo, C. Zhi, *Angew. Chem. Int. Ed.* **2025**, *64*, e202507724.
[49] W. Wang, J. Chen, E. C. M. Tse, *J. Am. Chem. Soc.* **2023**, *145*, 26678–26687.
[50] W. Liao, J. Wang, G. Ni, K. Liu, C. Liu, S. Chen, Q. Wang, Y. Chen, T. Luo, X. Wang, Y. Wang, W. Li, T.-S. Chan, C. Ma, H. Li, Y. Liang, W. Liu, J. Fu, B. Xi, M. Liu, *Nat. Commun.* **2024**, *15*, 1264.
[51] Z. Gong, X. Xiang, W. Zhong, C. Jia, P. Chen, N. Zhang, S. Zhao, W. Liu, Y. Chen, Z. Lin, *Angew. Chem. Int. Ed.* **2023**, *62*, e202308775.

Manuscript received: September 21, 2025
Revised manuscript received: November 29, 2025
Manuscript accepted: December 02, 2025
Version of record online: ■■, ■■